A Nearly Zero-Strain Li-Rich Rock-Salt Oxide with Multielectron Redox Reactions as a Cathode for Li-Ion Batteries

Ke Zhou,○ Yining Li,○ Yang Ha,○ Maojie Zhang, Walid Dachraoui, Haodong Liu, Chunyang Zhang, Xiangsi Liu, Fengchen Liu, Corsin Battaglia, Wanli Yang, Jianjun Liu,* and Yong Yang*

Abstract

Li-rich oxide cathodes are drawing increasing attention as next-generation cathode materials for the development of high-energy-density Li-ion batteries due to their strikingly high capacities. However, transition-metal migration, irreversible structural phase transformations, and the irreversible release of oxygen are responsible for rapid capacity and voltage decay. This study reports a Li-rich cation-ordered rock-salt oxide LixV0.4Ti0.4O2 (LVTO, x = 0.97/1.2) with space group $Fd\bar{3}m$ that delivers a high capacity of over 250 mAh g–1 and capacity retention up to 89% after 50 cycles. A comprehensive experimental analysis confirms that the capacity can be attributed to the reversible V3+/V5+ multielectron cationic redox reactions and a minor contribution from reversible anionic redox reactions. Importantly, LVTO exhibits nearly zero-strain behavior upon (dis)charge cycling cycles, which is associated with reversible V migration from octahedral to tetrahedral sites. Our results demonstrate that Li-rich rock-salt oxide LVTO could be a promising cobalt-free cathode material for Li-ion batteries.

1. Introduction

With the rapidly increasing deployment of Li-ion batteries (LIBs) in electric vehicles and grid-level energy storage systems, the demand for high-energy-density and low-cost cathode materials prompted extensive research activities. (1,2) Traditional layered transition-metal oxide electrodes (*e.g.*, $LiCoO_2$, $LiNi_{0.6}Co_{0.2}Mn_{0.2}O_2$, and $LiNi_{0.8}Co_{0.1}Mn_{0.1}O_2$) exhibit practical capacities of ≤190 mAh g^{-1}, which represents still less than 70% of their theoretical maximum capacity based on the redox of the transition metals (TMs). (3,4) Over the last decade, Li-excess layered oxides (*e.g.*, Li_2MnO_3, $Li[Li_xMn_yNi_zCo_{1-x-y-z}]O_2$, Li_2RuO_3, *etc.*) have attracted increasing interest as they demonstrated high capacities of more than 300 mAh g^{-1}, which exceed the theoretical capacity of the TMs redox process. (5) The origins of the extra capacity were discussed extensively, invoking over-oxidation of TMs, Li^+/H^+ exchange, lattice oxygen redox, interphase oxygen redox, *etc.* (6) It is now well accepted that both cationic and reversible anionic redox occurs in these high-capacity Li-excess layered oxides. (7) However, Li-excess layered oxides still suffer from severe capacity and voltage decay, and voltage hysteresis due to oxygen released during prolonged cycling and TM migration into vacant Li sites of the depleted Li layers, forming a more stable rock-salt structure to hinder Li^+ diffusion. (8,9)

Recently, Li-excess cation-disordered rock-salt oxides (DRX) with space group $Fm\bar{3}m$ were shown to deliver well over 250 mAh g^{-1}. (10) For example,

$Li_{1.3}Mn_{0.4}Nb_{0.3}O_2$ and $Li_2Mn_{2/3}Nb_{1/3}O_2F$ compounds have shown high discharge capacities around 300 mAh g^{-1}. (11,12) Furthermore, the DRX cathode material family allows a broad TM cation selection other than the critical Co, such as Ni^{2+}/Ni^{3+}, Ni^{2+}/Ni^{4+}, Mn^{3+}/Mn^{4+}, Mn^{2+}/Mn^{4+}, V^{3+}/V^{4+}, V^{4+}/V^{5+}, Cr^{3+}/Cr^{6+}, Mo^{3+}/Mo^{5+}, and Mo^{3+}/Mo^{6+}. (10,13,14) Nevertheless, rapid capacity and voltage decay, as well as pronounced voltage hysteresis is also observed in DRX materials due to oxygen release. In a typical DRX, such as $Li_{1.2}Mn_{0.4}Ti_{0.4}O_2$, the capacity retention reaches only 43% after 50 cycles. (13,15) Increasing the capacity associated with TM redox and decreasing the capacity associated with oxygen redox was shown to improve capacity and voltage retention without sacrificing high capacity. (16) For instance, Yabuuchi and co-workers reported that Mo-based DRX delivers ~280 mAh g^{-1} with a three-electron Mo^{3+}/Mo^{6+} redox reaction and negligible capacity fading during the first five cycles. (17) They further demonstrated that $Li_{1.25}Nb_{0.25}V_{0.5}O_2$ delivers a reversible capacity of over 200 mAh g^{-1} with a capacity retention of 98% after 20 cycles based on a two-electron V^{3+}/V^{5+} redox. (18,19) These results prove that multielectron redox reactions of TMs improve capacity retention by reducing the oxygen redox during cycling. Apart from high energy density, the rate capability is another critical factor for designing cathode materials for high-energy LIBs that still needs to be improved for DRX materials. (15,20)

Therefore, it remains important to explore novel cathode materials, which can offer stable structures and excellent electrochemical performances. Eum

et al. demonstrated that the O_2-structure $Li_x(Li_{0.2}Ni_{0.2}Mn_{0.6})O_2$ ($x \approx 0.83$) enables reversible intracycle TM migration and delivers relatively high capacity retention of ~82.5% after 40 cycles with good voltage retention. (21) Li et al. synthesized a layered-rock-salt-intergrown cathode displaying a high capacity of 244 mAh g^{-1} and low hysteresis during cycling with nearly zero-strain behavior in structure. (22) In addition, a series of V-based materials (Li_2VO_2F and $Li_2V_{0.5}Ti_{0.5}O_2F$) were reported by Chen et al. (23) and Baur et al. (24) They demonstrated that these materials could deliver a reversible capacity of 350 mAh g^{-1} with V^{3+}/V^{5+} two-electron redox. Motivated by the considerations above, we here synthesize a new class of Li-rich cation-ordered rock-salt oxides $Li_xV_{0.4}Ti_{0.4}O_2$ (LVTO, $x = 0.97$ for pristine, $x = 1.2$ for the electrode after the first cycle). Synchrotron X-ray diffraction (XRD), time-of-flight powder neutron diffraction (TOF PND), combined with transmission electron microscopy (TEM) prove that this oxide possesses a cation-ordered rock-salt structure with space group $Fd\bar{3}m$. The electrochemical analysis, V K-edge X-ray absorption spectroscopy (XAS), and solid-state nuclear magnetic resonance (ssNMR) spectroscopy confirm the two-electron redox process of the V^{3+}/V^{5+} couple. Besides the cationic redox processes, resonant inelastic X-ray scattering (RIXS) shows some minor contributions from reversible oxygen redox to the capacity. Furthermore, using *in situ* and *ex situ* XRD as well as density functional theory (DFT) calculations, we demonstrate that LVTO is stable upon high-capacity cycling without significant volume expansion/contraction. The nearly zero-strain

behavior is shown to be the result of reversible V ion migration between octahedral and tetrahedral sites, effectively compensating for volume expansion/contraction associated with (de)lithiation. Due to the V^{3+}/V^{5+} multielectron redox, minimal reversible oxygen redox, and good structural stability, LVTO is shown to exhibit a high reversible capacity over 250 mAh g^{-1} and capacity retention of 89% after 50 cycles.

2. Results and Discussion

2.1. Crystal Structure

According to inductively coupled plasma optical emission spectroscopy (ICP-OES), the actual composition of the prepared material is $Li_{0.97}V_{0.4}Ti_{0.4}O_2$ (as pristine Li-deficient LVTO), giving rise to metal valence increase, which will be discussed later. Figure S1a shows high-angle annular dark-field scanning transmission electron microscopy (HAADF-STEM) image of its particles. The shape of Li-deficient LVTO particles is irregular, and the average particle size is ~5 μm. Energy-dispersive X-ray spectroscopy (EDS) mapping of Li-deficient LVTO particles shows a uniform distribution of all of the elements (Figure S1b).

Synchrotron XRD (sXRD) and TOF PND patterns are shown in Figure 1a,b, respectively. All of the reflections in Figure 1a can be well indexed to a cubic cation-ordered rock-salt structure with space group $Fd\bar{3}m$. This structure is isostructural with cubic-$LiFeO_2$, $LiTi_2O_4$, $Li_2Ni_{1/3}Ru_{2/3}O_3$. (25−27) Rietveld refinements of both results indicate a good fit in the peak position based on

the $Fd\bar{3}m$ space group (see detailed information in Tables S1 and S2). In cation-ordered rock-salt structure (inset in Figure 1b), a part of Li shares 16d sites with V and Ti atoms, and the remaining part of Li shares the 16c sites with V (but not with Ti). (26,28)

Figure 1

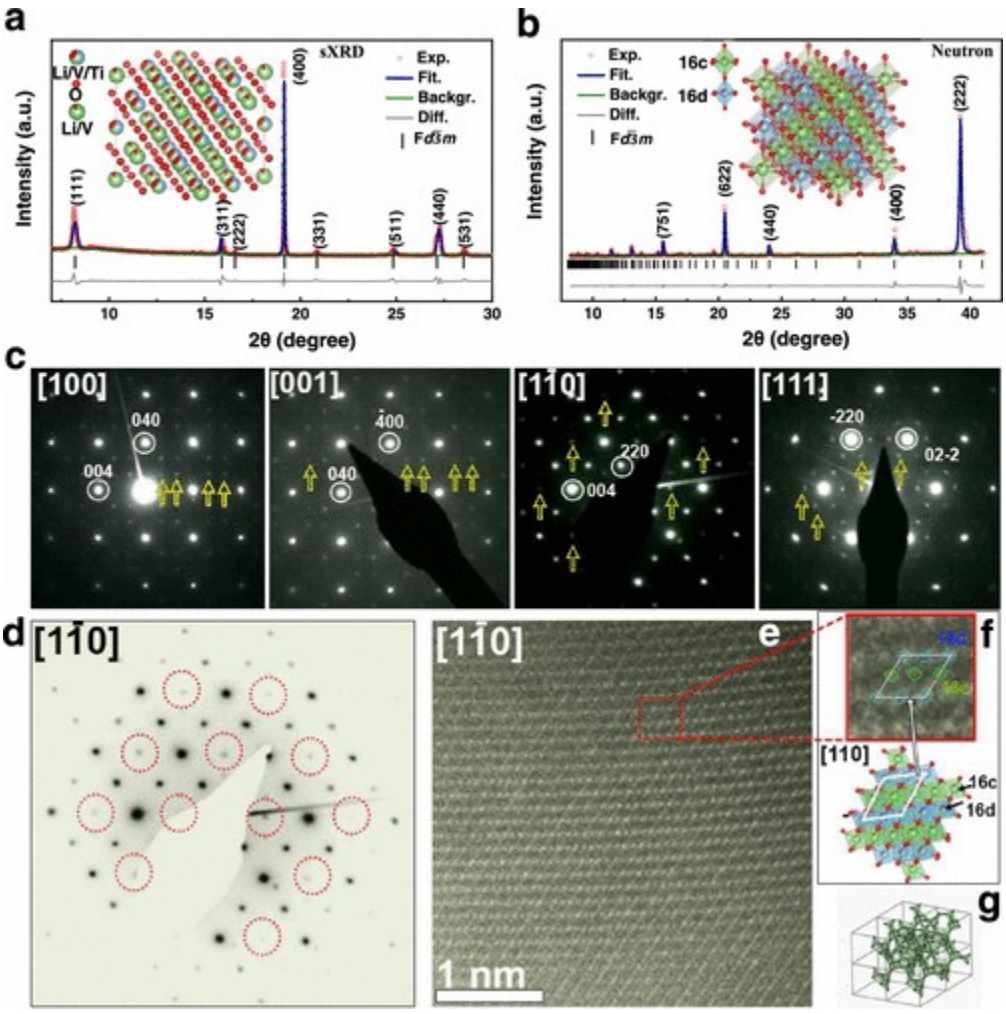

Figure 1. Li-deficient of cation-ordered rock-salt framework and advanced (S)TEM analysis. sXRD (a) and TOF PND (b) patterns of Li-deficient and the corresponding Rietveld refinement. The inset is the schematic diagram of the cation-ordered rock-salt structure. (c) Representative selected area electron

diffraction (SAED) patterns indexed in cubic structure with the space group $Fd\bar{3}m$, super-reflections are highlighted with yellow arrows. SAED pattern (d) along the $[1\bar{1}0]$ direction and its corresponding HAADF-STEM image (e) at atomic resolution. (f) Zoom-in on the right side corresponds to the zone designed by the red square and the atomic model is oriented along the $[1\bar{1}0]$ direction to show separately 16d and 16c sites. (g) Li diffusion pathways (marked by green bonds).

To further verify the cation-ordered rock-salt structure of Li-deficient LVTO, a TEM investigation was undertaken. The tilt series of selected area electron diffraction (SAED) was recorded from a large number of crystallites. Representative patterns are shown in Figure 1c. The set of strong reflections corresponds to the cubic structure in the $Fd\bar{3}m$ space group. In addition to the set of strong reflections, weak satellite reflections are observed along these directions (marked by yellow arrows). These are indexed by an ordered rock-salt structure, with a cation-ordered supercell, and have been reported in a layered cathode. (29,30) To determine the origin of these super-reflections and diffuse intensities HAADF-STEM was carried out. Since the high-resolution HAADF-STEM is a two-dimensional (2D) projection of the three-dimensional (3D) structure and based on the model shown in Figure 1b, the only projection that can show a separation of the 16d and 16c in 2D projection is the $[1\bar{1}0]$ zone axis. For that, we need to orient the crystals along the $[1\bar{1}0]$ direction and image it with atomic resolution. The HAADF-STEM image along the $[1\bar{1}0]$ direction is shown in Figure 1e with its

corresponding SAED pattern (Figure 1d), where the super-reflections related to the occupation of 16d sites by V and Ti are highlighted by red circles. The contrast obtained in the HAADF-STEM images is dominated by Rutherford scattering. Therefore, the scattered intensity scales are in good approximation with the atomic number Z^n of the elements, with n = 1.6–1.8. (31) If 16d sites were occupied only with Li, no contrast would be observed in HAADF-STEM images. However, one can see that the zoom-in in the top-right side of Figure 1f shows clearly spots at the locations corresponding to the 16d sites, which means that cations are occupying these sites. Since the occupancy of V in the 16c sites is around 6% and the occupancy of Ti and V in 16d sites is around 66% this will allow us to consider that the brighter spots in the HAADF-STEM image are related to the cations in 16d sites and the less bright ones are related to 16c sites (Table S2). The inset in the bottom-right of the image shows the atomic model projected along the $[1\bar{1}0]$ direction where the cations in 16d and 16c sites are highlighted. Thus, electron diffraction and high-resolution HAADF-STEM image confirm the TMs ordered rock-salt pattern. In addition, we observe that Li ions migrate through 3D channels in this rock-salt framework in Figure 1g, involving no face-sharing TM ion (represents 0-TM channel) to form a percolating network that is conducive to the Li transport, making it more efficient than 2D Li transport in traditional layered oxides. (32−34)

2.2. Electrochemical Characterization

Figures 2a and S2a show the voltage profiles of Li-deficient LVTO measured between 1.5 and 4.8 V at 30 mA g^{-1} and room temperature (RT) in half-cells *vs* Li metal. The initial charge and discharge capacities are 180 and 249 mAh g^{-1} with coulombic efficiency (CE) of 138% (Figure S2d), indicating part of Li in the anode (lithium metal) are supplemented to the cathode electrode at the end of the first cycle (1st). The ICP results of the cathode electrode after the first cycle show that the elemental composition is $Li_{1.2}V_{0.4}Ti_{0.4}O_2$ (Li-excess LVTO), forming our target oxide. Concurrently, the structure still maintains the cation-ordered rock-salt structure (Figure S3) and this material shows similar electrochemical curves in subsequent cycles. In addition, there is almost no capacity loss, and the reversible capacity is around 250 mAh g^{-1} (energy density 615 Wh kg^{-1}). Moreover, the discharge capacity increases gradually from 253 mAh g^{-1} (5th) to 276.5 mAh g^{-1} (20th) and maintains a high capacity retention of 89% after 50 cycles (50th) with stable CEs. The voltage decay over these 50 cycles is negligible (Figure S4a). Figures 2b and S2b present the voltage profiles at 300 mA g^{-1}, exhibiting a reversible capacity of 189 mAh g^{-1} and good capacity retention of 96% after 50 cycles. This CE fluctuates because of the excessively high current density (Figure S2e). We also investigated the performance of LVTO at a low temperature of 5 °C showing a reversible capacity of 184 mAh g^{-1} with nearly no capacity decay for 50 cycles (Figures 2c and S2c,f). Ultimately, Figure 2d shows high capacity retention of LVTO under different conditions. Figure 2e provides a comparison of the capacity retention after 10, 20, and 50 cycles of LVTO with

other DRX materials in the literature (Table S3), where LVTO exhibits higher capacity and better capacity retention. Differential capacity as a function of voltage (d*Q*/d*V*) plots are shown in Figure 2f. The charge process is characterized by three oxidation peaks at 2.6 V (Ox1), 3.5 V (Ox2), and above 4.0 V (Ox3) (indicated by the boxes). Furthermore, three major peaks in the discharge directions are observed at 3.3 V (Re1), 2.3 V (Re2), and 1.7 V (Re′). Besides the Ox3 and Re′ areas, the other areas are highly reversible in subsequent cycles. We assign V^{3+}/V^{4+} to Ox1 and Re2, V^{4+}/V^{5+} to Ox2 and Re1, and Ox3 to oxygen oxidation based on a common understanding. (35) The stability of these redox peaks in the d*Q*/d*V* profiles indicates the high cycling stability of LVTO.

Figure 2

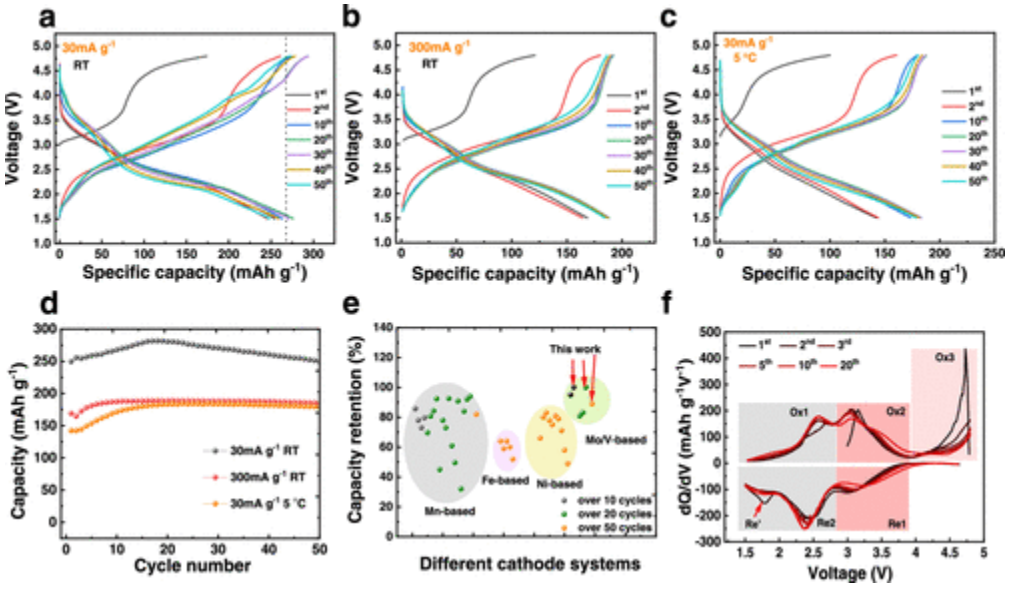

Figure 2. Galvanostatic cycling of LVTO between 1.5 and 4.8 V at different current densities and temperatures in half-cells *vs* Li metal: (a) 30 mA g^{-1} and room temperature (RT, 25 °C), (b) 300 mA g^{-1} and RT, and (c) 300 mA

g^{-1} and 5 °C. (d) Corresponding capacity *vs* cycle numbers. (e) Comparison of capacity retention over 10, 20, and 50 cycles between LVTO and a series of DRX cathode materials reported in the literature (a more detailed comparison is displayed in Table S3). (f) Differential capacity as a function of voltage (d*Q*/d*V*) for LVTO at a current density of 30 mA g^{-1} and RT.

The galvanostatic intermittent titration technique (GITT) is employed to record the initial and the second cycle to investigate the voltage hysteresis and kinetics at quasi-equilibrium in Figure S4b. Cells are rested for 30 min after each galvanostatic charge–discharge step with 20 mA g^{-1} for 20 min. A small overpotential of about 20–30 mV is observed during Ox1/Ox2 of the charge and Re1/Re2 of discharge associated with the oxidation and the reduction of V. A much larger overpotential of around 70–105 mV is observed during Ox3 and Re′ associated with lattice oxygen redox at high voltages and electrolyte decomposition. (36) Note that the large voltage hysteresis during Ox3 (high-voltage region) in the second cycle is alleviated compared to the first cycle. We calculate the Li-ion diffusion coefficient (D_{Li}) of the second charge process from GITT data (Figure S4c,d) from the voltage relaxation employing Fick's second law. (26) The D_{Li} value extracted for LVTO during the first and second charge process remains at 10^{-9} cm^2 s^{-1} up to 60% state of charge then drops rapidly to 10^{-13} cm^2 s^{-1} of 100% state of charge, ensuring its excellent performance at high current densities. These values are comparable to layered oxide cathode materials, while DRXs show values that are typically 2–4 orders of magnitude lower. (32) Therefore, we confirm

that the 3D pathways in the Li-rich cation-ordered rock-salt framework enable rapid transport of Li ions, promoting good rate capability and low-temperature performance.

2.3. Redox Mechanism

Multiple related techniques including X-ray absorption near-edge structure (XANES), high-efficiency RIXS, and soft X-ray absorption spectroscopy (sXAS) were used to probe the oxidation states of V and O at different states of (dis)charge in LVTO independently. The V K-edge XANES data at each state is shown in Figures 3a and S5a. The edge energies are plotted in Figure 3b and are compared with the reference of V_2O_3 (V^{3+}), VO_2 (V^{4+}), and V_2O_5 (V^{5+}) (horizontal red dashed lines) to estimate the V valence at each stage. The edge energy of the pristine state is similar to that of VO_2, revealing that the initial V's oxidation state is close to V^{4+}, not V^{3+}, which is consistent with the ICP results. Upon charging to 4.3 V (1st Ch4.3), the V edge shifts to higher energy, which is consistent with a higher oxidation state of V. When first charged to 4.8 V (1st Ch4.8), the edge energy shifts toward higher energies and is close to that of V_2O_5, implying that a large amount of the V^{4+} oxidizes to V^{5+}. This behavior is in sharp contrast with the DRXs with single-electron redox TM, which often exhibit lattice oxygen oxidation at this high voltage. (13,37) Upon discharge, the V edge shifts to lower energy. In particular, when fully discharged to 1.5 V (1st Dis1.5), the edge energy becomes similar to the energy of V^{3+} in V_2O_3. During the second charge, similar energy shifts ($V^{3+/4+}$ and $V^{4+/5+}$) corresponding to the two-electron

oxidation of V are observed. The V edge energy at 2nd Ch4.8 is slightly higher than that at 1st Ch4.8, which could be due to the reaction proceeds more completely during the charging of the second cycle. This also explains why the charge capacity of the second cycle is higher than the discharge capacity of the initial cycle. Our data suggest that V remains redox-active through the whole charge process enabling highly reversible cycling. Meanwhile, the ^{51}V solid-state nuclear magnetic resonance (ssNMR) spectra in Figure 3c further support the change of the V's oxidation state during the (dis)charge process. In the pristine sample, the ^{51}V resonance at −553 ppm has relatively low intensity, but when fully charged, exhibits the highest intensity, suggesting the presence of V^{5+}, as identified in the XAS experiments. After discharge to 1.5 V, the signal is invisible, which suggests that only V^{3+} paramagnetic ions remain.

Figure 3

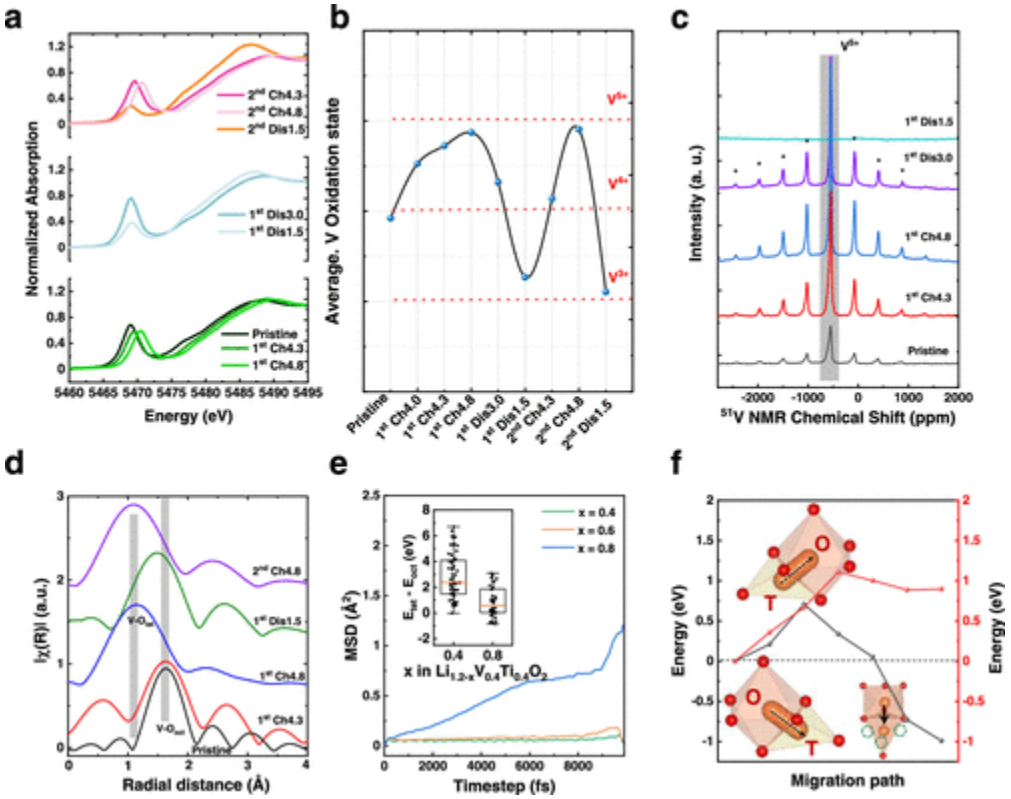

Figure 3. Redox mechanism of LVTO during electrochemical cycling. (a) *Ex situ* V K-edge XAS spectra at different (dis)charge states, (b) corresponding average V oxidation state evolution extracted from (a) and Figure S5a. (c) *Ex situ* ^{51}V MAS ssNMR spectra. (d) Fourier transform k^3–weighted V K-edge extended X-ray absorption fine structure (EXAFS) spectra. The peaks in the gray area represent the V–O coordination in octahedral (V–O_{oct}) and tetrahedral (V–O_{tet}). (e) Mean-square displacement (MSD) *vs* simulation time in delithiation process for $Li_{1.2-x}V_{0.4}Ti_{0.4}O_2$. The insets show the energy difference of V at the tetrahedral and octahedral sites at different delithiation states. (f) Diffusion energy barriers of V when passing through the octahedral (O)–tetrahedral (T) and tetrahedral (T)–octahedral (O) sites.

In addition, a notable change of the pre-edge peak intensity in V K-edge XANES spectra between 5467 and 5470 eV upon cycling can be observed, which is assigned to the symmetry change of the V site. (38) As shown in Figure 3d, the Fourier transform k^3-weighted EXAFS spectra of the pristine and 1st Ch4.3 state for LVTO display all of the V resides in octahedral sites with the V–O bonds. Once fully charged (1st Ch4.8), the majority of the V ions migrate to tetrahedral sites with shorter V–O bonds. Upon discharging to 1.5 V, most of the tetrahedral sites V reversibly migrate back to the octahedral sites. Similar V (and other TM) migration was also noted for other systems. (39,40) Also, the V L-edge XAS spectra (Figure S5b) show shifting to low energy upon charging, which cannot be explained solely by the V valence change. A simulation of the V L-edge for different oxidation states and ligand fields of VCl_x (3, 4, 5) shows that both the oxidation state and the ligand field have an impact on the L-edge spectra (Figure S6). It can be seen, that when changing from tetrahedral site to octahedral site, the absorption peaks do not necessarily shift to high energy with an increasing oxidation valence state of V, which is the same as our result. These simulations suggest that a change in the ligand field also needs to be taken into consideration in addition to the V redox. (41) Both the V K-edge XANES and L-edge sXAS, suggest that in LVTO, the coordination of V in the (dis)charged states is different, confirming that the migration of V ion causes a different coordination environment.

To further understand the diffusion paths and the kinetics of V ion migration, the mean-square displacements (MSDs) of all atoms in $Li_{0.4}V_{0.4}Ti_{0.4}O_2$ as a function of time are shown in Figure 3e. V atoms in the high delithiation ($x \approx 0.8$) exhibit by far the highest MSD slope among all states, which demonstrates that the V^{5+} ions in delithiated LVTO diffuse much faster than in pristine and half-charged LVTO. The insets show that the energy difference of V is low in the tetrahedral sites for $x \approx 0.8$, indicating that V^{5+} ions prefer the tetrahedral sites in this state. Figure 3f shows the diffusion energy barriers of V passing from an octahedral to a tetrahedral site. According to the nudged elastic band (NEB) method, the diffusion energy barrier for V ions for this transition is 0.7 eV, suggesting that it is kinetically feasible for V ions to migrate from the octahedral to tetrahedral sites. Furthermore, the energy barrier for the reverse path, *i.e.*, from a tetrahedral to octahedral site is 1.1 eV, which also suggests reversible migration of V ions, comparable to Ni^{n+} migration from the TM layer into the Li layer in layered cathodes. (42) At the same time, Figure S7 shows that V ions tend to migrate to the tetrahedral sites surrounded by Li vacancies. Therefore, the predicted migration mechanisms where V ions migrate to face-shared tetrahedral sites can explain the experimental findings as shown in Figure 4a. Ti K-edge XANES data is shown in Figure S5c. The edge energy shifts only by a very small amount, implying that Ti ions remain in the Ti^{4+} state during the cycling of LVTO. It was reported in the literature that reduction of Ti^{4+} to Ti^{3+} occurs

at ~1.7 V, (36) corresponding to Re′ in d*Q*/d*V* curves, so we conclude that a small amount of Ti^{3+} appears during the first discharge.

Figure 4

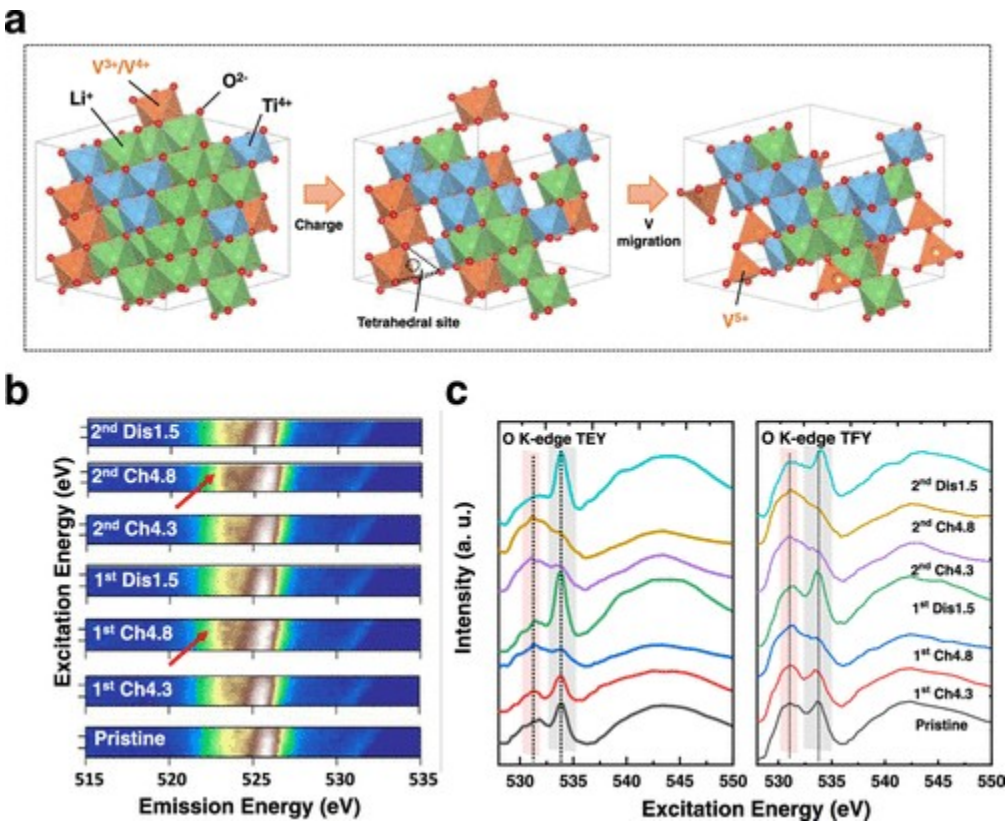

Figure 4. (a) Schematic of V ion migration during charging. (b) *Ex situ* O K-edge mapping of resonant inelastic X-ray scattering (mRIXS) at 531 eV excitation energy. The fingerprint oxidized oxygen feature (indicated by the red arrow) becomes more intense upon the charge in the first two cycles. (c) *Ex situ* O K-edge XAS spectra. Total electron yield (TEY) probes the surface, and total fluorescence yield (TFY) probes a depth of ~150 nm.

O K-edge RIXS proved to be a robust method to study O redox. The oxidized O species result in a conserved feature at ~531 eV excitation and ~524 eV emission on the 2D RIXS map. (43) As shown in Figures 4b (red arrow)

and S5d, O mapping of resonant inelastic X-ray scattering (mRIXS) and RIXS near 531 eV excitation energy show a small shoulder when the electrode is fully charged to 4.8 V (1st Ch4.8 and 2nd Ch4.8, Ox3), suggesting only a minimal amount of lattice O redox is present at high voltage in LVTO. *Operando* differential electrochemical mass spectrometry (DEMS) was also conducted to monitor the irreversible release of CO_2 gas (0.106 μmol mg^{-1}, Figure S5e), and no O_2 gas was detected. Previous work has reported that the source of CO_2 gas can be divided into two parts. For the low-voltage region (3.8–4.0 V), at least 70% of the CO_2 gas evolved the decomposition products of surface carbonate (*e.g.*, Li_2CO_3). The remaining gas in the high-voltage region (4.0–4.8 V) is derived from the excessive oxidation of oxidized O species with the decomposition products of the electrolyte. (15) Therefore, the DEMS result shows that for LVTO, there is still a certain amount of irreversible oxygen redox to form CO_2 gas and loss in the Ox3 region. Moreover, the O K-edge sXAS data of LVTO is shown in Figure 4c. The total electron yield (TEY) signal is surface-sensitive with a probe depth of ~10 nm. (44) The sharp feature at 534 eV is a fingerprint of CO_3^{2-}, which is often observed when the electrolyte reacts at the electrode surface. (45) In LVTO, the carbonate signal gradually decreases upon charging to 1st C4.8, shows up again during discharging, and maximizes at the end of discharge (1st Dis1.5). Such behavior is reproducible in the second cycle that followed. The trend is similar but less pronounced in the total fluorescence yield (TFY) signal, which has a deeper probe depth of ~150 nm. This suggests that

carbonate cycling mainly takes place at the electrode surface. It is noted that the theoretical capacity of LVTO is 268 mAh g^{-1} if only based on the two-electron V^{3+}/V^{5+} redox couple. This value is lower than the measured capacity of LVTO. Therefore, the additional capacity could be from lattice oxygen and carbonate (carbonate functional group, CO_3^{2-}) cycling, such as Li_2CO_3, $(CH_2OCO_2Li)_2$, *etc.* This surface carbonate cycling was also reported in a recent study on Li_2MnO_3. (46)

2.4. Structural Stability

In situ XRD and *ex situ* sXRD patterns for LVTO as a function of the (dis)charge states are analyzed in Figure 5. Figure 5a unveils that there is no new phase formed suggesting LVTO maintains the initial cation-ordered rock-salt framework during the initial cycle. The diffraction angles, as well as the peak intensities of the Bragg reflections of LVTO, remain almost unchanged. Furthermore, *ex situ* sXRD patterns (Figure 5b) also show the high structural stability of LVTO at different (dis)charge states since the calculated a-lattice parameters of LVTO increased by less than 0.01% compared to the pristine state (Figure S8). In the literature, conventional layered oxides and DRX oxides experience an irreversible anisotropic gradual change in lattice parameters during cycling. (5,47,48) After cycling LVTO for 5 and 50 cycles, the reflections still show only a slight shift compared to the pristine state, exhibiting nearly “zero-volume” changes or zero-strain characteristics upon (dis)charge cycling of LVTO. TEM images and the corresponding lattice fringe of LVTO are shown in Figure 5c. The lattice plane spacing of LVTO cycled for

5 and 50 cycles is almost the same as for the pristine sample. The SAED of the pristine electrode corresponds to the cation ordering rock-salt structure. The electrodes after 5 and 50 cycles, can still see the representing (400) plane (d = 0.20 nm) and the (400), (440), and (710) crystal planes, which are coincident with all XRD results.

Figure 5

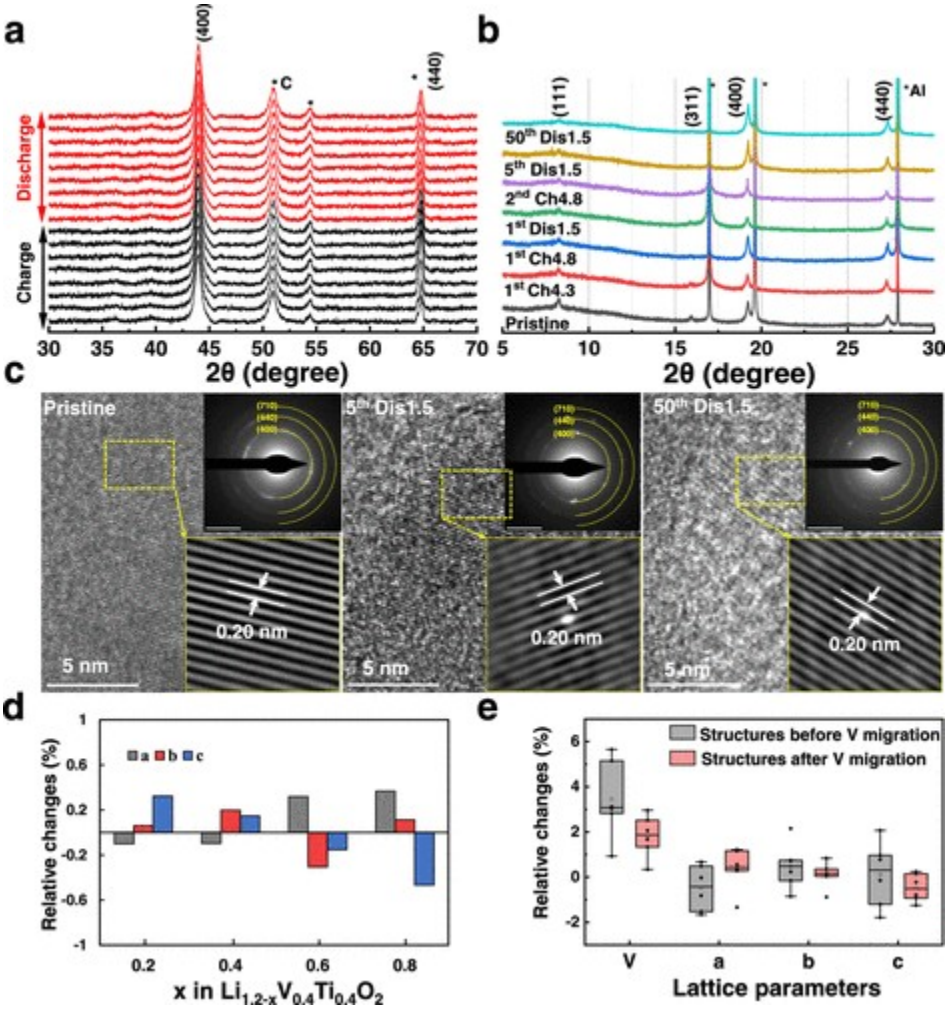

Figure 5. Crystal structure evolution during cycling. (a) *In situ* XRD patterns of LVTO during the first (dis)charge process. The symbols * represent the peaks of carbon (C) and aluminum (Al) current collectors, respectively. (b) *Ex*

situ sXRD patterns of LVTO with different (dis)charge states. (c) TEM images, the corresponding lattice fringe, and the SAED for the pristine LVTO and the electrodes after 5 and 50 cycles. The calculated relative changes of lattice parameters from DFT calculation in each delithiated state (d) and the structure of before and after V migration (e) for LVTO.

In addition, the calculated relative changes of lattice parameters of LVTO upon delithiation calculated by the density functional theory (DFT) calculation are also very small (less than 0.5%) than other layered cathode oxides (Figure 5d), (42,49) indicating the excellent structural stability of LVTO. This cation-ordered rock-salt structure is based on the $[B_2]O_4$ spinel framework, and the structure of $[B_2]O_4$ provides virtually no change to the lattice parameter. (50,51) Moreover, combined with the change of the pre-edge of the V K-edge XANES spectra and previous reports, (18,22,52) the migration of V ion would increase electrostatic interaction to resist the crystal lattice change in the lithium extraction process. (18) From these calculation results, it can be concluded that the lattice parameters after V migration are more stable than before V migration (Figure 5e). Thus, LVTO provides a rigid frame structure to achieve better electro-performance as a new cathode material.

3. Conclusions

In conclusion, using X-ray/neutron/electron diffraction, X-ray absorption spectroscopy, solid-state nuclear magnetic resonance spectroscopy, DFT

calculation, and electrochemical methods, we reveal the following main points: (i) The new Li-rich LVTO material displays a rock-salt framework with space group $Fd\bar{3}m$. (ii) The reversibility of V^{3+}/V^{5+} redox with the minimal anionic oxygen redox results in a high reversible capacity for LVTO. (iii) LVTO exhibits a nearly zero-strain behavior during cycling, which could be partly attributed to the reversible migration of V ions. As a result, this Li-rich rock-salt oxide exhibits a high reversible capacity, good rate capability, and capacity retention under different conditions. Our discovery gives a new strategy to design high-performance Li-rich cathodes for LIBs.